

PAPER

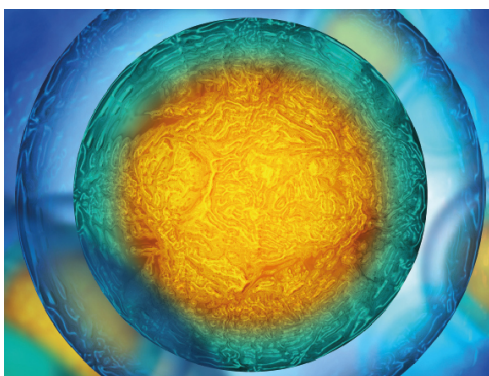
## Numerical modeling of a self-propelled dolphin jump out of water

To cite this article: Michel Bergmann 2022 *Bioinspir. Biomim.* 17 065010

View the [article online](#) for updates and enhancements.

### You may also like

- [Recent studies of the mortality and cancer morbidity experience of uranium workers and a fresh look at depleted uranium](#)  
Ronald L Kathren
- [Balancing the production line using the ergonomic approach](#)  
Rosnani Ginting, Muhammad Khatami and Alfin Fauzi Malik
- [SRP Meeting: Developments in Operational Health Physics, University of Birmingham, 25-26 March 1998](#)



Biophysical Society

IOP | ebooks™

Your publishing choice in all areas of biophysics research.

Start exploring the collection—download the first chapter of every title for free.

# Bioinspiration & Biomimetics



## PAPER

# Numerical modeling of a self-propelled dolphin jump out of water

RECEIVED  
10 June 2022

REVISED  
26 August 2022

ACCEPTED FOR PUBLICATION  
6 September 2022

PUBLISHED  
26 October 2022

Michel Bergmann\* 

Inria, Memphis Team, 200 Avenue de la Vielle Tour, 33450 Talence, France

IMB, Institut de Mathématiques de Bordeaux, 351 Cours de la Libération, 33405 Talence, France

\* Author to whom any correspondence should be addressed.

E-mail: [michel.bergmann@inria.fr](mailto:michel.bergmann@inria.fr)

**Keywords:** numerical simulation, biolocomotion, Navier–Stokes, fluid–structure interactions

## Abstract

A computational model is developed to investigate the jump of a self-propelled dolphin out of water. This model relies on the Navier–Stokes equations, where a fictitious domain approach with the volume penalization method is used for fluid–structure coupling, and the continuous surface force approach is used to model the water–air interface, the latter being tracked in a level-set framework. The dolphin’s geometry is based on freely available data from the literature. While body deformation is imposed, the leading linear and angular displacements are computed from Newton’s laws. Numerical simulations show that it is necessary to generate large propulsive forces to allow the jump out of water. When the dolphin is out of water, its trajectory follows a purely ballistic one.

## 1. Introduction

The study of underwater swimming animals is interesting with regards to understanding the possible effects related to evolution, in particular to make links between the geometry of the body, the unsteady nature of the flow, and the unsteady swimming deformations imposed by muscles. The latter can be optimized by using the energy enclosed in incoming vortices, in active (Gopalkrishnan *et al* 1994, Triantafyllou *et al* 2002, Liao *et al* 2003, Fish and Lauder 2006) or passive (Beal *et al* 2006) ways, or using vortices possibly generated by neighboring fishes (Bergmann and Iollo 2011, Maertens *et al* 2017, Gao and Triantafyllou 2018, Li *et al* 2022). Vortex-induced control by the caudal tails of vortices generated along the fish body (Zhu *et al* 2002) is also another mechanism to improve swimming efficiency. The drag reduction and thrust generation are linked to the generation of an inverse Von Kármán street, as observed for simple manipulated circular cylinder wake flow (Bergmann *et al* 2006).

A detailed comprehension of all these mechanisms may help to design new concepts of autonomous underwater vehicles (AUVs). The swimming of a fish has been considered, following the pioneering but controversial work of Gray (1936) (later called Gray’s

paradox), as being a very efficient means of locomotion. A review from a fluid mechanics point of view of Gray’s paradox can be found in Bale *et al* (2014). Also, this type of motion allows a maneuverability never reached by the previous generation of AUVs, of a torpedo type (Bozkurttas *et al* 2009).

As already mentioned, a dolphin’s kick in swimming is an efficient way to move in water. Human swimmers, especially during competitions, try to mimic a dolphin’s kick during the fully immersed stage (von Loebbecke *et al* 2009b, von Loebbecke *et al* 2009c). A comparison of humans and cetaceans is given in von Loebbecke *et al* (2009a).

The swimming of an animal in water is a complex and beautiful phenomenon that is easy to observe in nature, but difficult to model numerically. The complexity comes from the reciprocal coupling between the fluid and the animal’s body. This phenomenon is even more complex when the animal swims close to the surface, because it is necessary to take into account the deformation of the surface of the water and the forces related to surface tension. The complexity is greatest when the animal crosses the surface, typically when it jumps out of the water. High-performance propulsion together with trajectory control to optimize the position at the early jump are required to jump out of water. The jumping dynamics of a variety of aquatic animals are described in Chang *et al* (2019),

and a focus on the study of archer fish jumps can be found in Mendelson and Techet (2020). Examples of jump spinning (twist) maneuvering can be found in Fish *et al* (2006).

The goal of this paper is thus to study a dolphin jump in a numerical framework. Only a few numerical simulations of dolphin-like swimming have been reported in the literature, most of them are cited above. One reason is that it is difficult to define a realistic dolphin geometry. In this study, we will use the freely available geometry of the *Lagenorhynchus obliquidens* dolphin proposed in Tanaka *et al* (2019). The other reason is, as previously mentioned, the complexity of the numerical modeling. Indeed, it is necessary to model the unsteady fluid structure interactions with large interface deformations and possibly large density ratios (body and water interface deformations). In this study, we consider a fictitious domain approach where the computational mesh, i.e. grid nodes, does not necessarily follow the interfaces. The dolphin body is considered with the volume penalization (VP) method (Angot *et al* 1999), the fluid–structure interface is followed in a Lagrangian way, and the water–air interface is tracked in a Eulerian way using a level set function (Osher and Sethian 1988, Sethian 1999). Even if it is not a dominant force at the dolphin’s scale, we consider the surface tension using the continuous surface force (CSF) method originally introduced in Brackbill *et al* (1992). Other fictitious domain approaches can be used to compute large density ratios flows such as, for instance, the one recently proposed in Nangia *et al* (2019a, 2019b). For simplicity reasons, no skin effects are considered in this study, even if they can play an important role in passive drag reduction (Pavlov 2006).

The paper is organized as follows. After having introduced the modeling and numerical methods in section 2, including the description of the flow configuration, the governing equations, and the associated numerical schemes, we present the numerical results for dolphin jumps out of water in section 3. Some conclusions and perspectives are finally given in section 4.

## 2. Modeling and numerical methods

### 2.1. Flow configuration

A sketch of the flow configuration is given in figure 1. The whole domain is  $\Omega = \Omega_f^+ \cup \Omega_f^- \cup \Omega_s$ , where  $\Omega_s$  is the domain for the structure, i.e. the dolphin,  $\Omega_f^+$  is the domain filled with water, and  $\Omega_f^-$  is the domain filled with air. The two fluid domains are separated by an interface  $\Gamma_f$ , and the structure and the fluid domains are separated by an interface  $\Gamma_s$ . The intersection of  $\Gamma_f$  and  $\Gamma_s$  is noted as  $\Sigma_t = \Gamma_f \cap \Gamma_s$ . For three-dimensional problems,  $\Sigma_t$  could be a line, usually called the triple line. The external boundary of the domain is noted as  $\Gamma_e$ . In what follows, the

domain  $\Omega$  is a three-dimensional Cartesian box, and the external boundary is  $\Gamma_e = \Gamma_{\text{top}} \cup \Gamma_{\text{bottom}} \cup \Gamma_{\text{left}} \cup \Gamma_{\text{right}} \cup \Gamma_{\text{front}} \cup \Gamma_{\text{back}}$ , where each boundary is defined as indicated by the subscripts. The density of the dolphin is  $\rho_s$ , the density and dynamic viscosity of water are  $\rho^+$  and  $\mu^+$ , and the density and dynamic viscosity of air are  $\rho^-$  and  $\mu^-$ .

The different domains and interfaces introduced before also depend on time, and are mathematically defined by two level-set (Osher and Sethian 1988, Sethian 1999) scalar functions  $\psi_f$  and  $\psi_s$ . Here, the structure is arbitrarily defined by  $\psi_s > 0$ , the interface  $\Gamma_s$  by  $\psi_s = 0$ , and the fluids (water and air) by  $\psi_s < 0$ . Similarly, the water is arbitrarily defined by  $\psi_f > 0$ , the interface  $\Gamma_f$  by  $\psi_f = 0$ , and the air by  $\psi_f < 0$ .

### 2.2. Governing equations

Without loss of generality, the density  $\rho \in \mathbb{R}$  and dynamic viscosity  $\mu \in \mathbb{R}$  of the fluids can be written as:

$$\rho \equiv \rho(\psi_f) = \rho^- + H(\psi_f)(\rho^+ - \rho^-), \quad (1)$$

$$\mu \equiv \mu(\psi_f) = \mu^- + H(\psi_f)(\mu^+ - \mu^-), \quad (2)$$

where  $H$  is the Heaviside function, i.e.  $H(x < 0) = 0$ ,  $H(x > 0) = 1$ , and we can define  $H(x = 0) = 0.5$ .

The velocity field is  $\mathbf{u} \in \mathbb{R}^3$ ,  $p \in \mathbb{R}$  is the pressure field, and  $\mathbf{g} \in \mathbb{R}^3$  is the gravity acceleration vector. The viscous part of the stress tensor is  $D(\mathbf{u}) = \frac{\nabla \mathbf{u} + \nabla^T \mathbf{u}}{2}$ . In what follows, we note  $\mathbf{u} = (u, v, w)$ , where  $u$ ,  $v$ , and  $w$  denote the velocity components in the  $x$ ,  $y$ , and  $z$  directions, respectively. The incompressible Navier–Stokes equations for both fluids in domain  $\Omega_f^+ \cup \Omega_f^-$  are:

$$\frac{\partial \mathbf{u}}{\partial t} + (\mathbf{u} \cdot \nabla) \mathbf{u} = -\frac{1}{\rho} \nabla p + \frac{1}{\rho} \nabla \cdot 2\mu D(\mathbf{u}) + \mathbf{g} \text{ in } \Omega_f^+ \cup \Omega_f^-, \quad (3)$$

$$\nabla \cdot \mathbf{u} = 0 \quad \text{in } \Omega_f^+ \cup \Omega_f^-, \quad (4)$$

with initial conditions  $\mathbf{u}(\mathbf{x}, t = 0) = \mathbf{u}_0$  and  $p(\mathbf{x}, t = 0) = p_0$ , boundary conditions on the external boundary for velocity  $\mathbf{u}(\mathbf{x}, t)$  and pressure  $p(\mathbf{x}, t)$  for  $\mathbf{x} \in \Gamma_e$ , boundary conditions on the structure boundary  $\Gamma_s$ , and conditions through the bi-fluid interface  $\Gamma_f$ .

On the fluid–structure interface  $\Gamma_s$ , we have:

$$\mathbf{u}(\mathbf{x}, t) = \widehat{\mathbf{u}}(\mathbf{x}, t) \quad \text{on } \Gamma_s, \quad (5)$$

where the velocity  $\widehat{\mathbf{u}}(\mathbf{x}, t)$  will be described later on.

Two jump conditions also have to be satisfied throughout the bi-fluid interface  $\Gamma_f$ . The first kinematic condition is:

$$[\mathbf{u}] = 0 \quad \text{through } \Gamma_f. \quad (6)$$

The second dynamic jump condition traduces the equilibrium between pressure forces, the friction forces, and surface tension:

$$[-pI + 2\mu D(\mathbf{u})] \cdot \mathbf{n} = \sigma \kappa \mathbf{n} \quad \text{through } \Gamma_f, \quad (7)$$

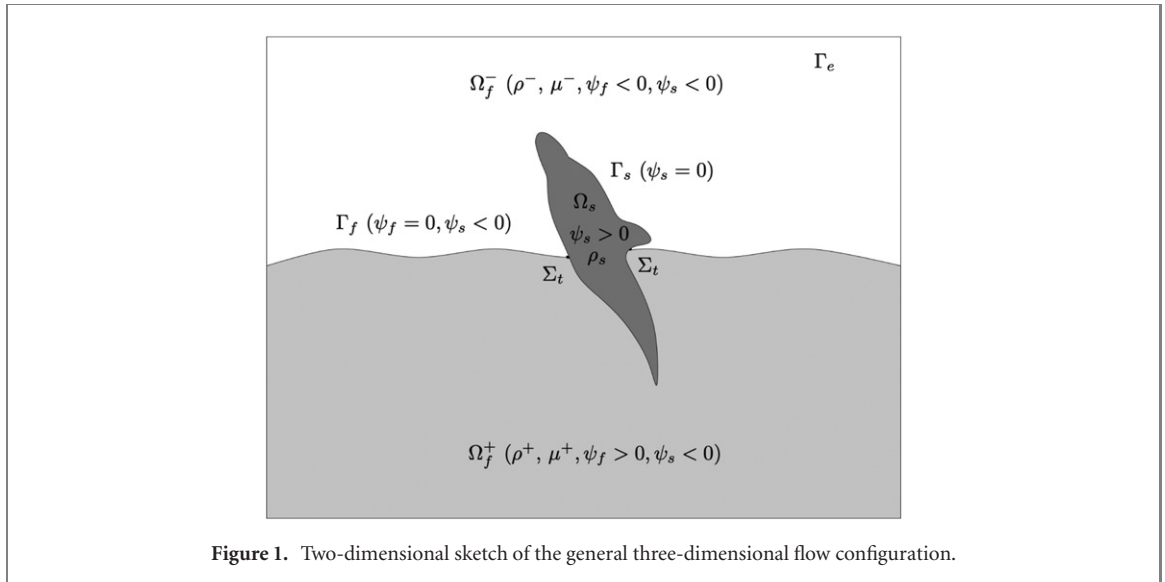


Figure 1. Two-dimensional sketch of the general three-dimensional flow configuration.

where  $\sigma$  is the value of the surface tension,  $\kappa$  is the curvature of the interface  $\Gamma_f$ , and  $\mathbf{n}$  is the unit normal to the interface  $\Gamma_f$  pointed to the air.

### 2.3. Fictitious domain approach

The numerical resolution of the Navier–Stokes equations (3) and (4) requires a discretization on a mesh. The difficulty is that the interfaces  $\Gamma_f$  and  $\Gamma_s$ , and thus the domains  $\Omega_f^+$ ,  $\Omega_f^-$ , and  $\Omega_s$ , are time-dependent. Different approaches to take into account interface conditions (5)–(7) can be envisioned.

This first class of methods is based on body-fitted grids. In these methods, degrees of freedom are put on the interfaces, and it is thus possible to impose directly the interface conditions (5)–(7). Mesh deformation can be handled with an arbitrary Lagrangian–Eulerian method. These methods are accurate, but require mesh adaptation and a mesh partitioning for parallel computations.

A second class of methods, which is adopted in this study, is based on fictitious domain approaches. In these approaches, the interfaces and associated domains do not cover the same mesh nodes at each time step: the interface can cross a fixed mesh, and no interface markers are thus required. Simple meshes like Cartesian ones can be used. The drawback is that the accuracy at interfaces can be degraded, and extra work has to be performed to model the interfaces.

The goal of fictitious approaches is to add extra force-like terms in the momentum equation (3) to take into account conditions (5)–(7). The condition on the fluid–structure interface is modeled with an extra term  $\mathbf{s}$  and the two conditions on the bi-fluid interface are modeled with the extra term  $\mathbf{f}$ .

The system (3)–(7) is thus recast in a system written in the whole domain  $\Omega$ :

$$\frac{\partial \mathbf{u}}{\partial t} + (\mathbf{u} \cdot \nabla) \mathbf{u} = -\frac{1}{\rho} \nabla p + \frac{1}{\rho} \nabla \cdot 2\mu D(\mathbf{u}) + \mathbf{g} + \mathbf{s} + \mathbf{f} \quad \text{in } \Omega, \quad (8)$$

$$\nabla \cdot \mathbf{u} = 0 \quad \text{in } \Omega. \quad (9)$$

The methods used to model the terms  $\mathbf{s}$  and  $\mathbf{f}$  have been inspired by the immersed boundary method (IBM) introduced by Peskin (1972). In this continuous framework, an infinite force applied on a Dirac support function is regularized around the interface. This is mainly done for numerical reasons that will be explained later on.

In this study, the fluid structure interface is modeled using the VP introduced in Angot *et al* (1999) section 2.3.1, and the bi-fluid interface with surface tension is modeled using the CSF method introduced in Brackbill *et al* (1992) section 2.3.2.

#### 2.3.1. Modeling of the conditions on the fluid–structure interface $\Gamma_s$

Among the most popular fictitious approaches are the IBMs originally introduced in Peskin (1972) and later on used in several studies (Mittal and Iaccarino 2005, Mittal *et al* 2008, Shirgaonkar *et al* 2009) and the VP method introduced in Angot *et al* (1999) and used, for instance, in biolocomotion problems (Bergmann and Iollo 2011, Bergmann *et al* 2014b, Bergmann and Iollo 2016). Another approach combining IBM and VP has been developed in Bergmann *et al* (2014a). Here, we use the VP method with

$$\mathbf{s} = \frac{\chi}{K} (\hat{\mathbf{u}} - \mathbf{u}), \quad (10)$$

where  $K \ll 1$  is the penalization parameter,  $\chi = H(\psi_s)$  is the characteristic function, and  $\hat{\mathbf{u}}$  is the velocity of the body (on the boundary and inside the body). In domain  $\Omega^\pm$ , we have  $\psi_s < 0$  and thus  $\chi = 0$ , and the Navier–Stokes equations are recovered. In

domain  $\Omega_s$ , we have  $\psi_s > 0$ , and thus  $\chi = 1$ , and the dominant term in (3) is  $\frac{\chi}{K}(\hat{\mathbf{u}} - \mathbf{u})$  leading to  $\mathbf{u} \rightarrow_{K \rightarrow 0} \hat{\mathbf{u}}$  in  $\Omega_s$ . Here, we chose  $K = 10^{-8}$ . The computation of  $\hat{\mathbf{u}}$  will be detailed in section 2.5.

### 2.3.2. Modeling of the conditions on the bi-fluid interface $\Gamma_f$

The CSF (continuum surface force) was originally introduced in Brackbill *et al* (1992) and developed in Sussman *et al* (1994). The CSF is to model the surface tension term as an extra volume force  $\mathbf{f}$  in the momentum equation. The jump,

$$[-pI + 2\mu D(\mathbf{u})] \cdot \mathbf{n} = \sigma \kappa \mathbf{n} \text{ through } \Gamma_f, \quad (11)$$

is considered in an integral form and we have:

$$\mathbf{f} = \frac{1}{\rho} \sigma \kappa \delta \mathbf{n}, \quad (12)$$

where  $\sigma$  is the surface tension,  $\kappa$  is the curvature of the interface,  $\mathbf{n}$  is the normal to the interface pointing to the air, and  $\delta$  is the Dirac distribution.

The normal  $\mathbf{n}$  and the curvature  $\kappa$  are:

$$\mathbf{n} = \frac{\nabla \psi_f}{\|\nabla \psi_f\|}, \quad (13)$$

$$\kappa = \nabla \cdot \left( \frac{\nabla \psi_f}{\|\nabla \psi_f\|} \right). \quad (14)$$

The problem is relaxed by regularization of the Dirac distribution  $\delta$  in a narrow band with width  $\epsilon$

$$H^\epsilon(\psi_f) = \begin{cases} 0 & \text{si } \psi_f < -\epsilon, \\ \frac{1}{2} \left( 1 + \frac{\psi_f}{\epsilon} + \frac{1}{\pi} \sin\left(\frac{\pi \psi_f}{\epsilon}\right) \right) & \text{si } |\psi_f| \leq \epsilon, \\ 1 & \text{si } \psi_f > \epsilon. \end{cases} \quad (15)$$

The regularized Dirac distribution is:

$$\begin{aligned} \delta^\epsilon(\psi_f) &= \frac{dH^\epsilon(\psi_f)}{d\psi_f} \\ &= \begin{cases} 0 & \text{si } |\psi_f| > \epsilon, \\ \frac{1}{2\epsilon} \left( 1 + \cos\left(\frac{\pi \psi_f}{\epsilon}\right) \right) & \text{si } |\psi_f| \leq \epsilon. \end{cases} \end{aligned} \quad (16)$$

The extra term due to the surface tension is thus finally

$$\mathbf{f} = \frac{1}{\rho} \sigma \kappa \delta^\epsilon \mathbf{n}. \quad (17)$$

Finally, due to the continuous framework introduced beforehand, the jump  $[\mathbf{u}] = 0$  through  $\Gamma_f$  in equation (6) is naturally satisfied.

### 2.4. Interface tracking

The model will be closed with computations of functions  $\psi_s$  and  $\psi_f$ . The definition of these functions is not unique, and due to its hyper-regularity we chose  $\psi_f$  to be the signed distance function, i.e.

$\|\nabla \psi_f(\mathbf{x})\| = 1 \forall \mathbf{x}$ . Let  $d(\mathbf{x}) \geq 0$  be the minimal distance from a given point  $\mathbf{x}$  to the interface  $\Gamma_f$ ; we have:

$$\begin{cases} \psi_f(\mathbf{x}) = 0 & \text{if } \mathbf{x} \in \Gamma_f, \\ \psi_f(\mathbf{x}) = +d & \text{if } \mathbf{x} \in \Omega_f^+, \\ \psi_f(\mathbf{x}) = -d & \text{if } \mathbf{x} \in \Omega_f^-. \end{cases} \quad (18)$$

The same holds for  $\psi_s$ . The signed distance allows us to simplify the computation of the normal and the curvature of the interface, and to determine in a more precise way the distance  $\epsilon$  defining the narrow band for CSF regularization.

These interfaces, represented by functions  $\psi_f$  and  $\psi_s$ , can be transported in Eulerian or Lagrangian ways. Due to possible large deformations and break downs, the bi-fluid interface  $\Gamma_f$  will be defined with a level set function that is able to track such an interface with topology changes. The level set  $\psi_f$  is thus transported by:

$$\frac{\partial \psi_f}{\partial t} + \mathbf{w} \cdot \nabla \psi_f = 0 \text{ in } \Omega_f^\pm, \quad (19)$$

where  $\mathbf{w}$  can be any desired velocity fields satisfying  $\mathbf{w}(\mathbf{x}, t) = \mathbf{u}(\mathbf{x}, t) \forall \mathbf{x} \in \Gamma_f$ . For simplicity reasons, we chose  $\mathbf{w}(\mathbf{x}, t) = \mathbf{u}(\mathbf{x}, t) \forall \mathbf{x} \in \Omega$ , but other choices like the extension velocities can be used (Adalsteinsson and Sethian 1999).

The signed distance behavior of the function  $\psi_f$  can be lost integrating (19), and it is thus necessary from time to time to reinitialize  $\psi_f$  to recover the signed distance function  $\|\nabla \psi_f(\mathbf{x})\| = 1$ . One of the most popular algorithms is the first-order fast marching (Sethian 1996, Sethian 1999), extended later to higher orders (Ahmed *et al* 2011).

Another class of method was introduced by Sussman (Sussman *et al* 1994). The goal is to solve a partial differential equation to recover the property  $\|\nabla \psi_f(\mathbf{x})\| = 1$ . This relaxation method is:

$$\frac{\partial \psi_f}{\partial \tau} + \text{sign}(\psi_f^0)(|\nabla \psi_f| - 1) = 0, \quad (20)$$

$$\psi_f(\mathbf{x}, \tau = 0) = \psi_f^0 = \psi_f(\mathbf{x}, t), \quad (21)$$

for a temporal horizon  $0 \leq \tau \leq \tau_F$  such that  $|\nabla \psi_f(\mathbf{x}, \tau_F)| = 1$ . The sign function is

$$\text{sign}(\psi_f) = \begin{cases} 1, & \text{if } \psi_f > 0, \\ 0, & \text{if } \psi_f = 0, \\ -1, & \text{if } \psi_f < 0, \end{cases} \quad (22)$$

or a regularized version of it.

In what follows, the dolphin surface  $\Gamma_s$  will be approximated by a mesh (i.e. with markers), and it is thus more convenient to use a Lagrangian transport for any mesh point  $\mathbf{x}_h$ :

$$\frac{d\mathbf{x}_h}{dt} = \hat{\mathbf{u}}_h. \quad (23)$$

The definition and computation of  $\hat{\mathbf{u}}$  will be defined in section 2.5.

The signed distance function is recovered computing the minimal distance to the interface:

$$\psi_s(\mathbf{x}) = \min_{\mathbf{y} \in \Gamma_s} \|\mathbf{x} - \mathbf{y}\|_2 S(\mathbf{x}), \quad (24)$$

where  $S(\mathbf{x})$  denotes the sign applied on a point  $\mathbf{x}$ , with  $S(\mathbf{x}) > 0$  inside the body, and  $S(\mathbf{x}) < 0$  outside. This sign function can be computed with simple geometric arguments, from the outward normal to the body.

The triple line  $\Sigma_t$ , defined as being the intersection between  $\Gamma_s$  and  $\Gamma_f$ , has to be modeled. Indeed, without special treatment, due to the non-slip boundary condition on  $\Gamma_s$ , the line would never move on  $\Gamma_s$ . In this study, we chose the macroscopic model introduced by Cox (1986). A local force proportional to the deviation of the equilibrium angle (Patankar 2003) is added to allow a displacement of the triple line.

Finally, since the flows under consideration are turbulent, a turbulence model introduced in Vreman (2004) is added.

## 2.5. Dolphin model

The geometry of the Dolphin is built from the *stl* file given in the supplementary material of Tanaka *et al* (2019). Indeed, the authors have performed a very productive work and have given a lot of material to work with. The geometry is reproduced in figure 2. The two first figures are the exact geometry given by Tanaka *et al* (2019), and the two last figures are the geometry slightly remodeled to fit our numerical framework with a regular surface mesh.

The body velocity is

$$\hat{\mathbf{u}}(\mathbf{x}, t) = \bar{\mathbf{u}}(\mathbf{x}, t) + \mathbf{u}^\theta(\mathbf{x}, t) + \tilde{\mathbf{u}}(\mathbf{x}, t) \quad \forall \mathbf{x} \in \Omega_s, \quad (25)$$

where  $\bar{\mathbf{u}}(\mathbf{x}, t)$  is the linear velocity,  $\mathbf{u}^\theta(\mathbf{x}, t)$  is the angular velocity, and  $\tilde{\mathbf{u}}(\mathbf{x}, t)$  is the deformation velocity. While the deformation  $\tilde{\mathbf{u}}(\mathbf{x}, t)$  has to be imposed by swimmer muscles, the linear and angular velocities are the results of the loads generated by the fluid on the body, and are computed from Newton's laws.

In order to avoid adding extra forces and torques due to deformation, a Procrustes analysis is performed. The deformation must not introduce any linear and angular displacements. We thus compute the linear and angular displacements induced by the imposed deformation, and subtract them to the final admissible deformations. This is actually done in figure 4.

The deformation velocity  $\tilde{\mathbf{u}}(\mathbf{x}, t)$  can be easily computed following surface markers in a Lagrangian way, after having performed the Procrustes analysis. To recover  $\tilde{\mathbf{u}}(\mathbf{x}, t)$  values in  $\Omega_s$ , interpolation is performed from values at the boundary  $\Gamma_s$ .

The swimming law is defined by a deformation of the swimmer midline, also called the backbone. As we will see later on, the dolphin jump can be decomposed in three steps.

- The first is an underwater generation of a propulsive force using periodic swimming with a large amplitude and frequency.
- The second corresponds to the jump out of the water, i.e. when the dolphin is in the air: the dolphin just imposes (active or passive) a constant curvature along the midline.
- The third and last step is another periodic swimming law with a small amplitude when the dolphin is back in the water.

We consider a backbone deformation in the plan  $(0, x, y)$  of the third figure in figure 2, where point  $O$  is at the front head of the dolphin and  $x$  positive to the right. Moreover, we consider that the midline for the steady body is  $0 \leq x \leq \ell$ ,  $y = 0$ , where  $\ell$  is the length of the swimmer.

Most fishes impose the following periodic swimming law (Barrett *et al* 1999):

$$y(x, t) = a(x) \sin(kx - \omega t), \quad (26)$$

with a constant phase velocity  $c_p = \omega/k$ , where  $k = 2\pi/\lambda$  is the wavenumber, corresponding to wavelength  $\lambda$ ,  $\omega$  is the circular frequency of oscillations, and  $a(x)$  is the envelope defined by  $a(x) = A/2 (c_0 + c_1(x-1) + c_2(x^2-1))$ . Other kinds of swimming laws can be found in Smits (2019) and Han *et al* (2020). The maximal tail amplitude  $A/2$  is an important parameter for swimming (Lighthill 1970). Here, we chose  $c_0 = 1$ ,  $c_1 = -0.825$ , and  $c_2 = 1.625$  for a unit length fish with  $0 \leq x \leq 1$ . These parameters are used to mimic a thunniform-like swimming. Several midline deformations are presented in figure 3 for one stroke, with  $A = 0.33$ .

Instead of directly imposing the swimming law (26), it is simpler to impose a curvature  $\kappa(s)$  along the midline with a curvilinear abscissa  $s$ . The curvature corresponding to the swimming law  $y(s, t) = a(s)\sin(ks - \omega t)$  for the first and third stage of the jump is:

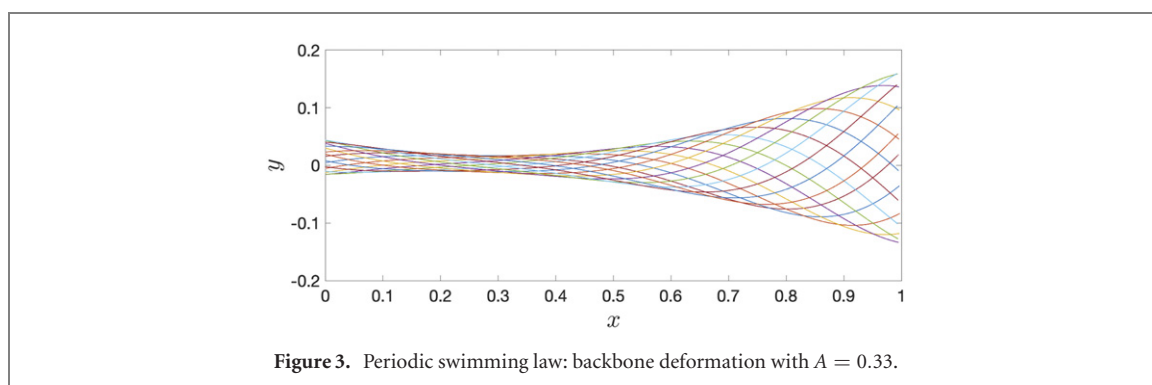
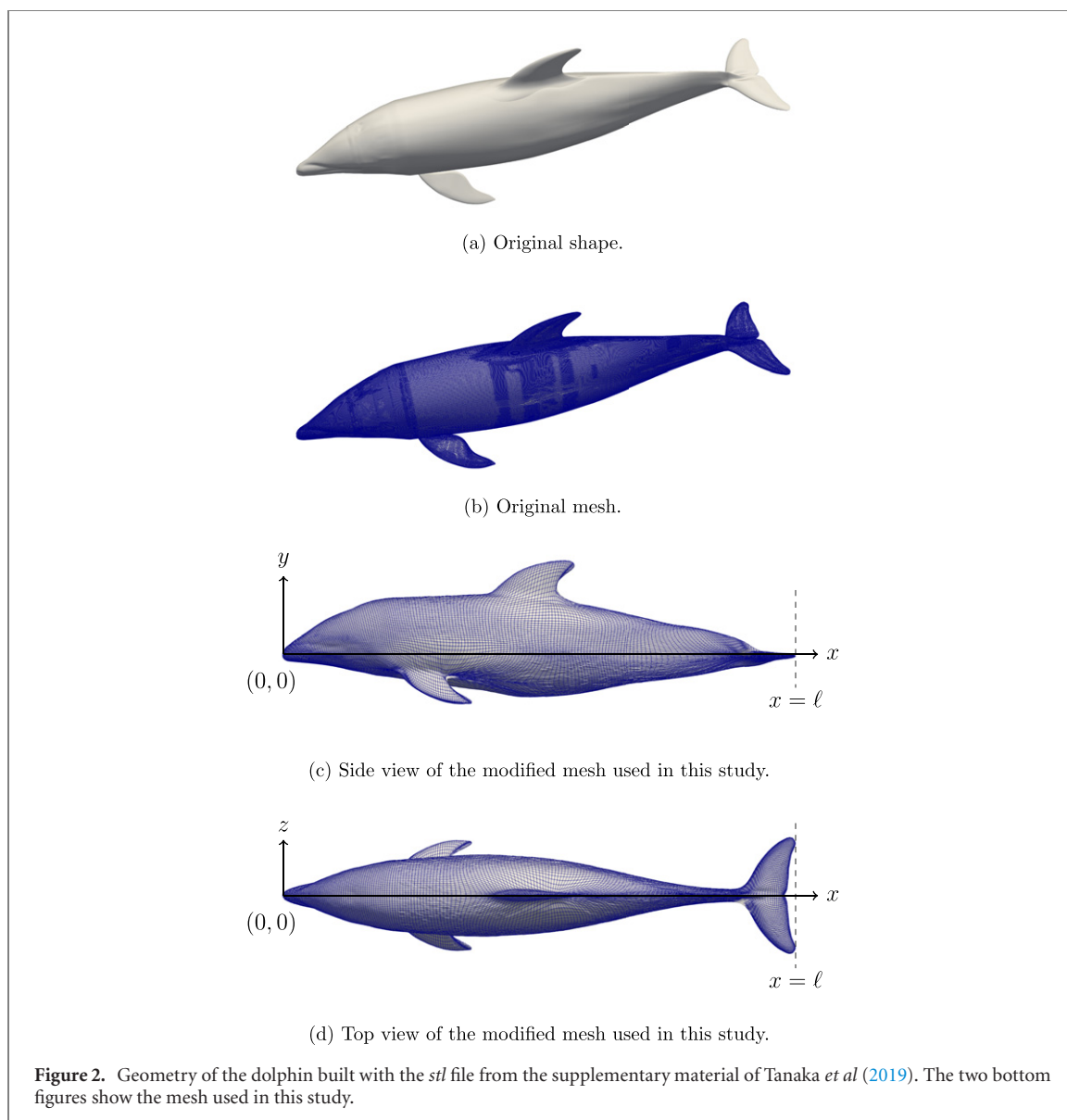
$$\kappa(s, t) = \frac{\frac{\partial^2 y}{\partial s^2}}{\left(1 + \left(\frac{\partial y}{\partial s}\right)^2\right)^{\frac{3}{2}}}. \quad (27)$$

The general curvature imposed on the midline is:

$$\kappa(s, t) = p(t)\kappa(s, t) + q(t)\bar{\kappa}, \quad (28)$$

where  $\bar{\kappa}$  is the curvature imposed for the jump, i.e. when the dolphin is in the air, and  $0 \leq p(t) \leq 1$  and  $0 \leq q(t) \leq 1$  are two functions, possibly piecewise defined, allowing us to go smoothly from step 1 to step 2 and from step 2 to step 3.

This swimming law is applied to the dolphin's midline (the backbone). All body surface mesh nodes



are displaced with respect to Euler Bernoulli beam deformation, i.e. each orthogonal section to the backbone for the undeformed shape remains orthogonal to the backbone during the deformation. Eight

snapshots of the deformed body shape corresponding to (28) over one periodic stroke ( $p = 1$  and  $q = 0$ ) are presented in figure 4. Note that a Procrustes analysis is performed.

Finally, the linear and angular motions are obtained from Newton's law

$$\begin{cases} m \frac{d\bar{\mathbf{u}}}{dt} = \mathbf{F}_{\text{ext}}, \\ \frac{dJ\boldsymbol{\omega}}{dt} = \mathbf{M}_{\text{ext}}, \end{cases} \quad (29)$$

where  $m$  and  $J$  are the mass and inertia matrix of the dolphin, and  $\bar{\mathbf{u}}$  and  $\boldsymbol{\omega}$  denote the linear and angular velocities.

The forces and the torques are computed by

$$\mathbf{F}_{\text{ext}} = - \int_{\Gamma_s} \mathbb{T}(\mathbf{u}, p) \mathbf{n} \, d\mathbf{x} + \mathbf{g}, \quad (30)$$

$$\mathbf{M}_{\text{ext}} = - \int_{\Gamma_s} \mathbf{r} \wedge \mathbb{T}(\mathbf{u}, p) \mathbf{n} \, d\mathbf{x}, \quad (31)$$

where  $\mathbb{T}(\mathbf{u}, p) = -p\mathbf{I} + \mu(\nabla\mathbf{u} + \nabla\mathbf{u}^T)$  is the stress tensor,  $\mathbf{n}$  is the unit outward vector to  $\Gamma_s$ , and  $\mathbf{r} = \mathbf{x} - \mathbf{x}_G$  with  $\mathbf{x}_G$  the dolphin's center of mass. The rotation velocity is given by  $\mathbf{u}^\theta = \boldsymbol{\omega} \wedge \mathbf{r}$ .

Note that other methods can be used to compute the forces and torques in a fictitious domain approach when no surface markers are available. For instance, the surface integrals in (30) and (31) can be transformed in control volume integrals (Nangia *et al* 2017).

## 2.6. Numerical resolution

The Navier–Stokes equations (8) and (9), and associated equations like transport and reinitialization of the level set function, are discretized in space on a uniform Cartesian mesh using a finite differences method. The temporal discretization of the Navier–Stokes equations is based on a fractional step method introduced in Chorin (1968) and Temam (1969). The numerical method used in this paper follows our previous work (Bergmann and Iollo 2011, Bergmann *et al* 2014a, Bergmann *et al* 2014b, Bergmann and Iollo 2016) and we thus recall only the main steps.

All the differential operators are discretized in space using centered second-order schemes, except the convective terms where up-winding is necessary for stability reasons. The convective terms in the momentum equations are discretized with a classical third order finite differences scheme, while the convective term in the level set transport equation (19) is discretized with a WENO5 (weighted essentially non-oscillatory) scheme (Liu *et al* 1994, Jiang and Shu 1996). A total variation diminishing third order Runge–Kutta (RK3-TVD) scheme is used to discretize equation (19) in time. The reinitialization equation (20) is solved using the subcell fix method proposed in Russo and Smereka (2000) with extensions developed in Luddens *et al* (2015). It is not necessary to perform a reinitialization step at each time step, and we use the criterion introduced in Luddens *et al* (2015) to decide when it is necessary to perform a reinitialization of the level set function.

The integrals over  $\Gamma_s$  involved to evaluate the forces and torques are discretized using the body surface mesh (that is a tessellation of the surface  $\Gamma_s$ ). Since the dolphin's surface mesh nodes do not coincide with the fluid mesh, the stress tensor is interpolated from fluid mesh to the body surface mesh.

## 2.7. Numerical validations

The numerical approach presented above has already been validated onto several benchmark problems in our previous publications. Several validations in three dimensions complement numerous validations already performed for two-dimensional problems. Our previous validations consider mono-fluid problems, i.e. without a bi-fluid interface. A first validation is the sedimentation of a sphere (Bergmann *et al* 2014b) for several sphere diameters and fluid viscosities. For bio-inspiration problems involving large deformations, another validation was performed in Bergmann and Iollo (2016) onto an eel swimming, originally proposed by Kern and Koumoutsakos (2006) and studied numerically thereafter in Bhalla *et al* (2013, 2014). For both validation problems, the numerical results are in good agreement with the reference ones.

In what follows, a three-dimensional bi-fluid validation is performed for the entry of a sphere into water. This problem has been studied experimentally (Aristoff *et al* 2010, Truscott *et al* 2014) and numerically with the commercial software ABAQUS in Ahmadzadeh *et al* (2014).

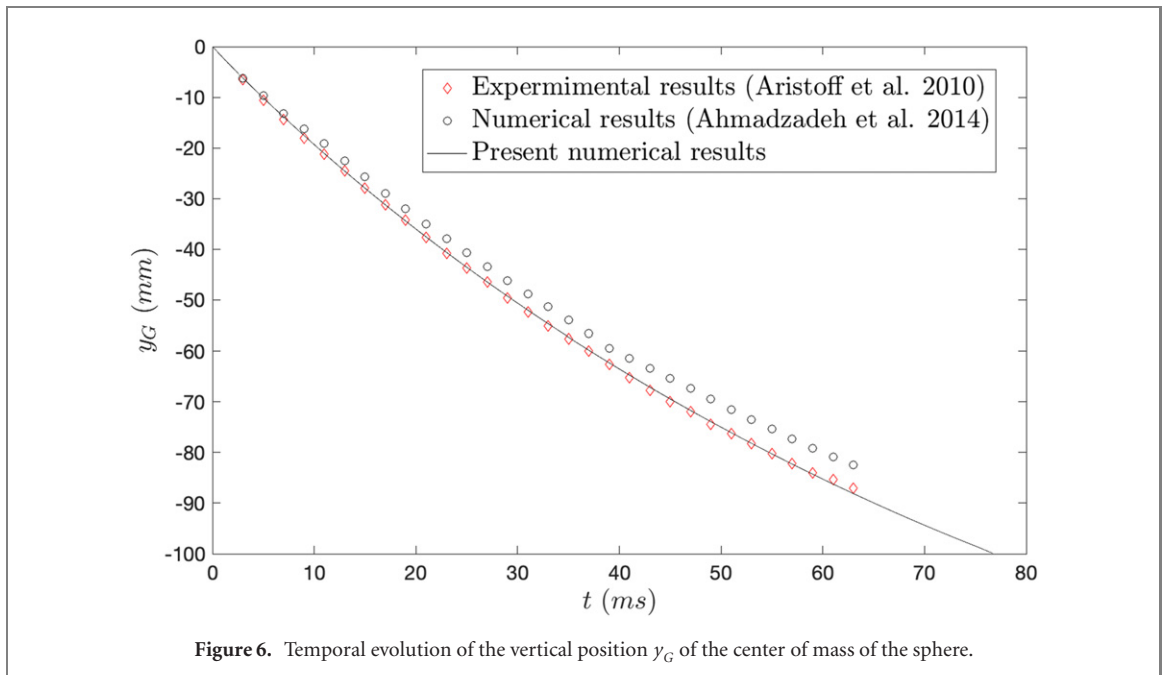
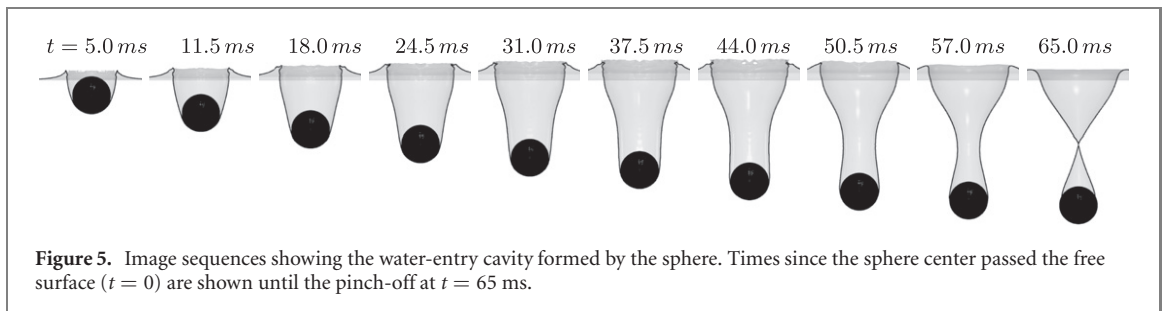
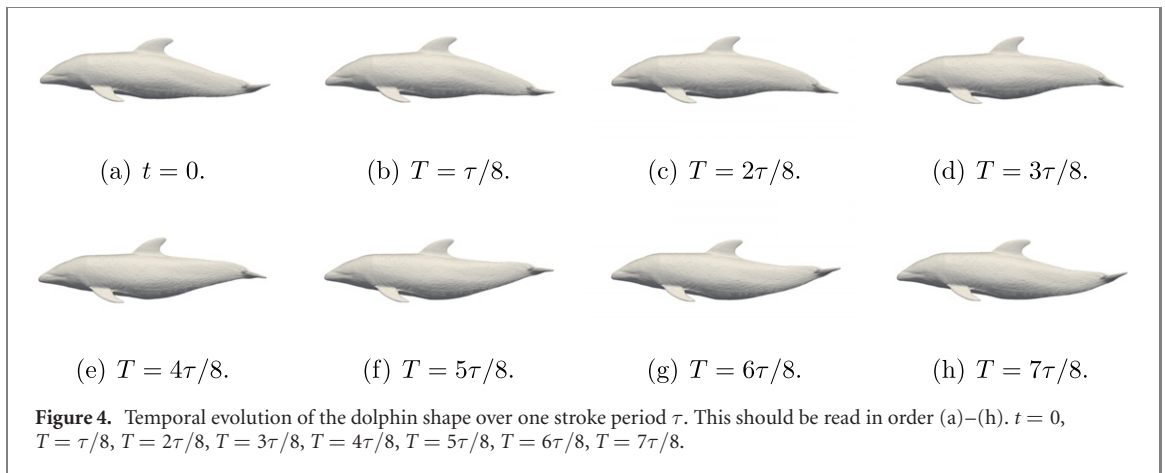
A sphere with diameter  $D = 0.0254$  m impacts the surface of the water at  $V_0 = 2.17$  m s<sup>-1</sup>. The density of the sphere is  $\rho_s = 1.14\rho^+$ . The densities and dynamic viscosities of the fluids are  $\rho^+ = 1000$  kg m<sup>-3</sup> and  $\mu^+ = 10^{-3}$  Pa s for the water, and  $\rho^- = 1.2$  kg m<sup>-3</sup> and  $1.87 \times 10^{-5}$  Pa s for the air. The surface tension is  $\sigma = 0.0728$  N m<sup>-1</sup>.

The computational domain under consideration is a Cartesian box with  $x \in [-6, 6]$  cm,  $y \in [-20, 10]$  cm, and  $z \in [-6, 6]$  cm. At rest, the air–water interface  $\Gamma_f$  is located at  $y_1 = 0$  cm, and the initial position of the center of mass of the sphere is  $\mathbf{x}_G = (x_G, y_G, z_G) = (0, D/2, 0)$  m.

The computational domain is discretized by  $240 \times 600 \times 240 \approx 35 \times 10^6$  cells, and the step size is  $h = \Delta x = \Delta y = \Delta z = 0.05$  cm. The time step is defined with a CFL (Courant–Friedrichs–Lewy) condition equal to 0.3. Non-slip boundary conditions are applied on all external boundaries. The flow is initially at rest, i.e.  $\mathbf{u}(0, \mathbf{x}) = \mathbf{0}$ .

Figure 5 presents the image sequences showing the water-entry cavity formed by the sphere until  $t = 65$  ms where the pinch-off, which is characterized by a cavity closure event, occurs. The results are in good agreement with the experimental results (Aristoff *et al* 2010) where the pinch-off is observed at  $t = 63.5$  ms,





and with the numerical results (Ahmadzadeh *et al* 2014) where the pinch-off is observed at  $t = 64.9$  ms.

A time history comparison of experimental (Aristoff *et al* 2010), numerical ABAQUS simulation (Ahmadzadeh *et al* 2014), and the present numerical results of sphere center depth are shown in figure 6. The present numerical results are in good agreement with the reference results, especially with the experimental ones.

### 3. Numerical results

#### 3.1. Numerical configuration and parameters

The densities and dynamic viscosities of the fluids are  $\rho^+ = 1000 \text{ kg m}^{-3}$  and  $\mu^+ = 10^{-3} \text{ Pa s}$  for the water, and  $\rho^- = 1.2 \text{ kg m}^{-3}$  and  $1.87 \times 10^{-5} \text{ Pa s}$  for the air. The surface tension is  $\sigma = 0.0728 \text{ N m}^{-1}$ .

The dolphin geometry is extracted from the supplementary material from Tanaka *et al* (2019) and the

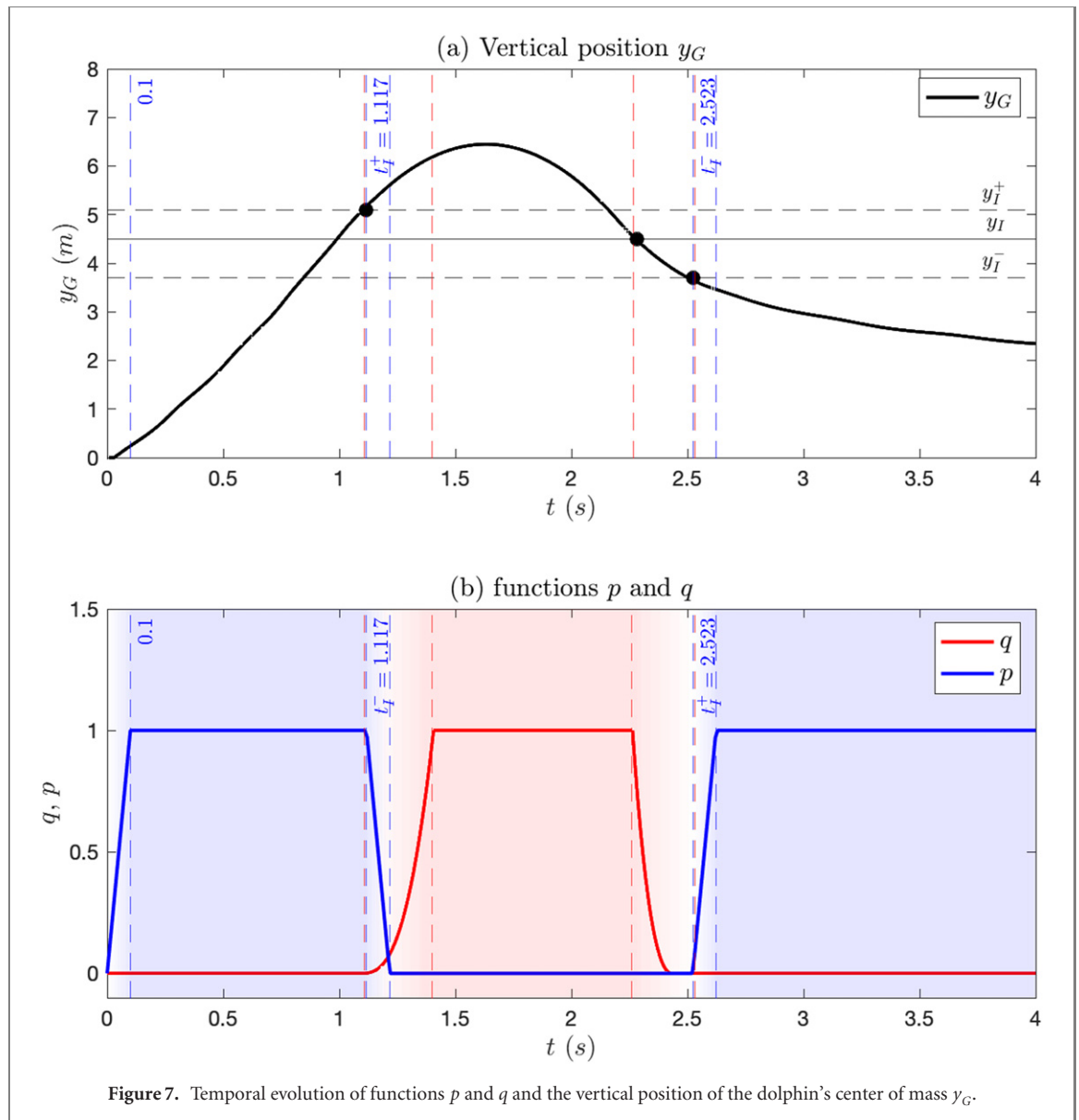


Figure 7. Temporal evolution of functions  $p$  and  $q$  and the vertical position of the dolphin's center of mass  $y_G$ .

geometry is reproduced in figure 2. Here, the length of the dolphin is imposed to be  $\ell = 3$  m, leading to a total mass  $m = 316$  kg with  $\rho_s = 1000$  kg m<sup>-3</sup>.

The computational domain under consideration is  $x \in [-12, 4]$  m,  $y \in [-3, 9]$  m, and  $z \in [-2, 2]$  m. At rest, the air–water interface  $\Gamma_f$  is located at  $y_I = 4.5$  m, and the center of mass of the dolphin is  $\mathbf{x}_G = (x_G, y_G, z_G) = (0, 0, 0)$  m. The initial orientation of the dolphin is  $\boldsymbol{\theta} = (\theta_x, \theta_y, \theta_z) = (0, 0, \theta_0)$ . While the initial angular velocity is  $\boldsymbol{\omega} = \mathbf{0}$ , the initial dolphin linear velocity is  $\bar{\mathbf{u}} = (u_G, v_G, w_G) = (0, v_0, 0)$ , where  $v_0$  can be a positive constant to decrease the distance to reach a sufficient velocity for a real jump, and thus to decrease the size of the computational domain.

The velocity boundary condition on the external boundaries  $\Gamma_{\text{ext}}$  is as follows. On the side boundaries (left, right, front, back), periodic conditions are imposed,  $\mathbf{u}_{\text{front}} = \mathbf{u}_{\text{back}}$  and  $\mathbf{u}_{\text{left}} = \mathbf{u}_{\text{right}}$ . No slip boundary conditions are imposed on the bottom

$\mathbf{u}_{\text{bottom}} = (0, 0, 0)$ , and the streamline type of boundary conditions are imposed on the top, i.e.  $v_{\text{top}} = 0$ ,  $\frac{\partial u_{\text{top}}}{\partial y} = \frac{\partial w_{\text{top}}}{\partial y} = 0$ .

The dolphin surface is discretized with a regular mesh composed by  $200 \times 200 = 40\,000$  cells (see the two bottom figures in figure 2). Even if large skewness of mesh near the fins and tails is observed, the mesh is a tessellation of the body surface on which integrals (30) and (31) can be discretized. This mesh is similar to those used in Bergmann and Iollo (2016) and Bergmann *et al* (2014b) for carangiform and thunniform swimmers.

The computational domain is discretized by  $640 \times 480 \times 160 \approx 50 \times 10^6$  cells, and the step size is  $h = \Delta x = \Delta y = \Delta z = 0.025$  m. The time step is defined with a CFL condition equal to 0.3.

Due to the large dolphin deformations, boundary layers are detached and it is thus not necessary to use a costly boundary layer mesh. The turbulence model introduced in Vreman (2004) is used. Other

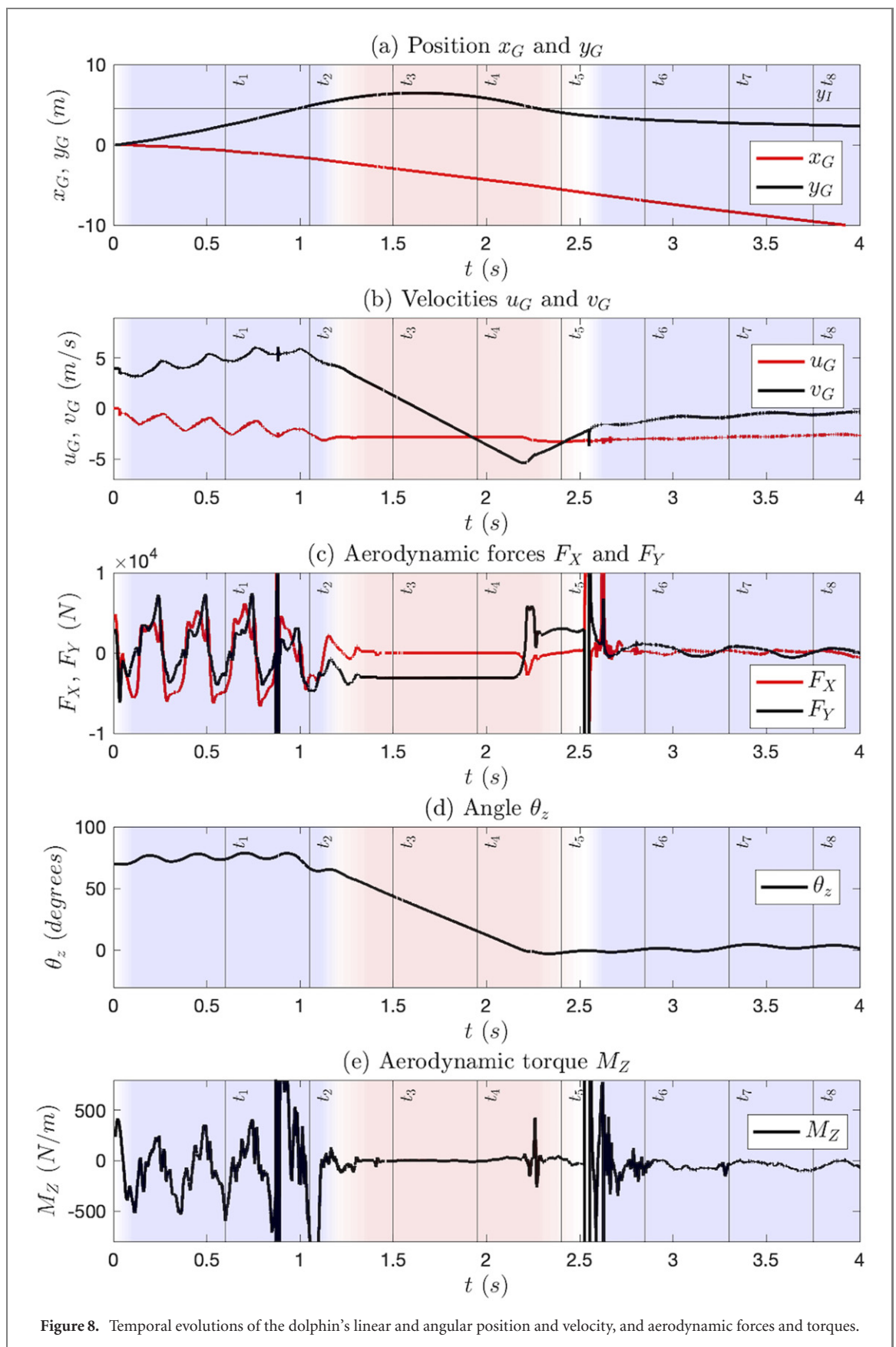
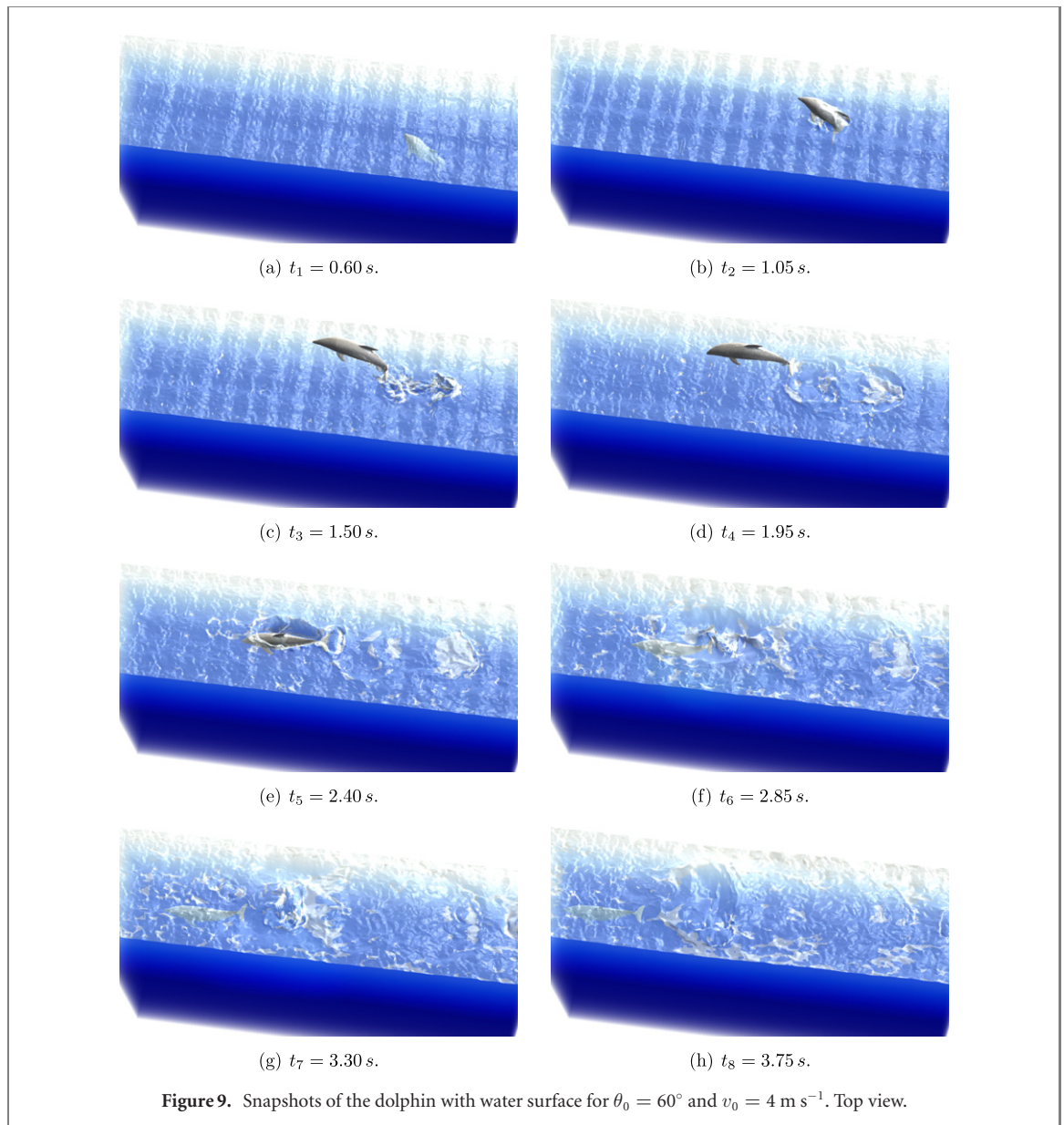


Figure 8. Temporal evolutions of the dolphin's linear and angular position and velocity, and aerodynamic forces and torques.



**Figure 9.** Snapshots of the dolphin with water surface for  $\theta_0 = 60^\circ$  and  $v_0 = 4 \text{ m s}^{-1}$ . Top view.

turbulence models may be used to study the laminar-turbulence transition (Riedeberger and Rist 2012).

Artificial waves at the air–water interface are generated by a Kelvin–Helmholtz instability using initial conditions  $u(\mathbf{x}, 0) = 0 \text{ m s}^{-1}$  in the water ( $\mathbf{x} \in \Omega_f^+$ ) and  $u(\mathbf{x}, 0) \neq 0 \text{ m s}^{-1}$  in the air ( $\mathbf{x} \in \Omega_f^-$ ).

From the initial water surface position at  $y_I = 4.5 \text{ m}$ , we define two other locations: the first one is over water,  $y_I^+ = y_I + 0.6 \text{ m}$ , and the second one is under water,  $y_I^- = y_I - 0.8 \text{ m}$ . We denote by  $T = 0.2 \text{ s}$  a transition period over  $p$  that goes linearly from 0 to 1 or from 1 to 0.

The dolphin's body deformation is defined according to the following swimming law.

(a) In order to produce enough propulsive effect to get out of the water, starting only 4.5 m under the surface, we imposed a sinusoidal law with large amplitude and frequency, i.e.  $A = 1.5 \text{ m}$  and  $f = \omega/(2\pi) = 4 \text{ Hz}$ , with an initial linear transition

of  $p(0) = 0$  and  $p(T) = 1$ . This swimming law is performed until the dolphin's center of mass  $y_G$  reaches  $y_I^+$  at time  $t_I^+$ , and we thus have  $p(t) = 1 \forall t \in [T, t_I^+]$ . The periodic swimming law is then linearly damped to reach  $p(t_I^+ + T) = 0$ .

(b) When the periodic swimming is damped from  $t = t_I^+$ , a mean curvature  $\bar{\kappa} = 1/R$  with  $R = 2 \text{ m}$  is progressively added to the whole midline. The smoothing function  $q$  depends on the vertical position of the center of mass such that maximal curvature is obtained when the dolphin is in the air. When  $y_G = y_I$  at the end of the jump, the function  $q$  is damped and the curvature tends to decrease to zero.

(c) When the dolphin re-enters the water due to gravity, more precisely when  $y_G < y_I^-$  at  $t = t_I^-$ , another periodic swimming with  $A = 1 \text{ m}$  and  $f = 2 \text{ Hz}$  is activated with a linear transition, with  $p(t_I^-) = 0$  and  $p(t) = 1$  for  $t \geq t_I^- + T$ .

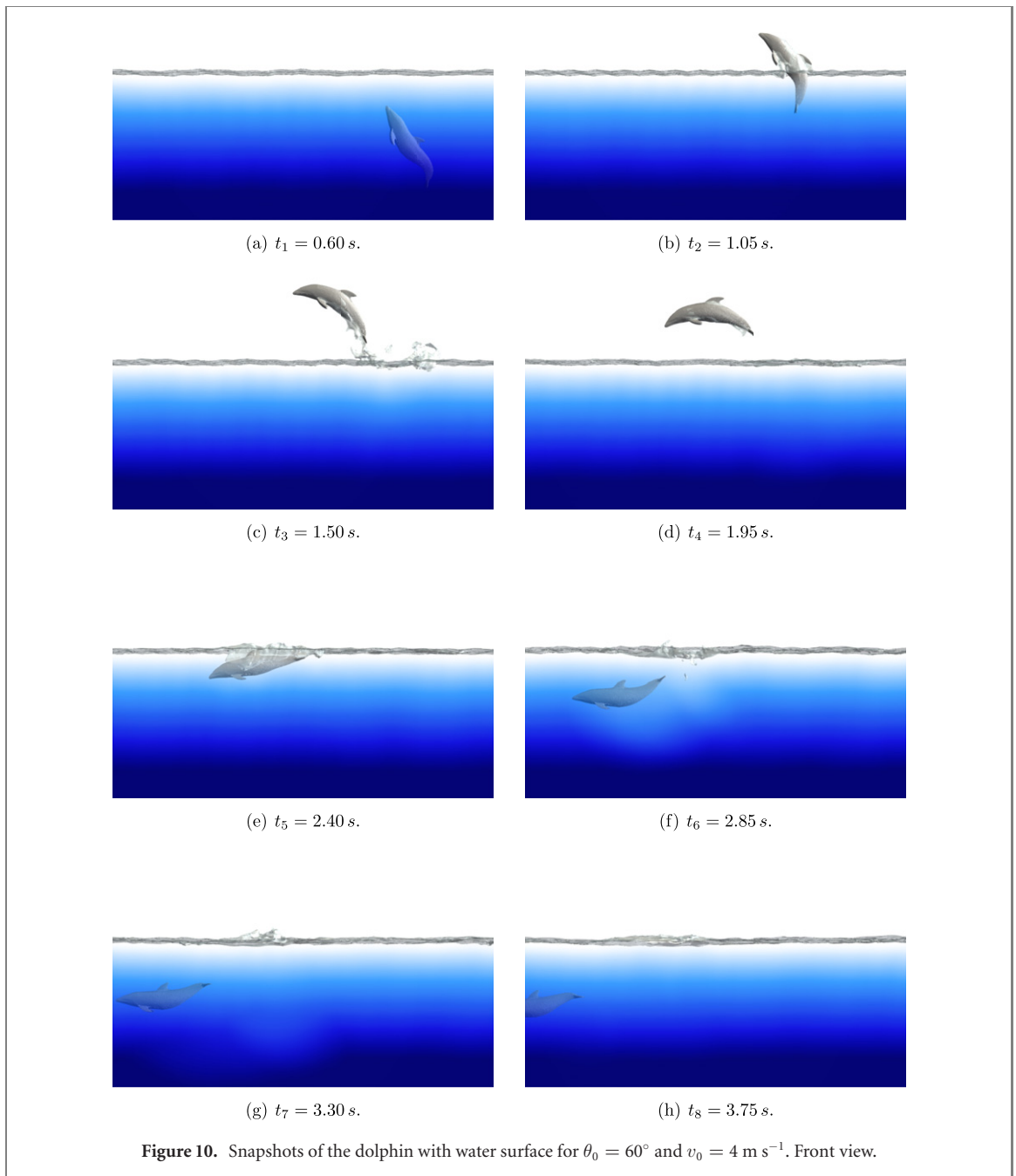


Figure 10. Snapshots of the dolphin with water surface for  $\theta_0 = 60^\circ$  and  $v_0 = 4 \text{ m s}^{-1}$ . Front view.

Mathematically, the function  $p$  depends on some temporal intervals defined by:

$$p(t) = \begin{cases} t/T & \text{if } 0 \leq t < T, \\ 1 & \text{if } T \leq t < t_I^+, \\ (t_I^+ + T - t)/T & \text{if } t_I^+ \leq t < t_I^+ + T, \\ 0 & \text{if } t_I^+ + T \leq t < t_I^-, \\ (t - t_I^-)/T & \text{if } t_I^- \leq t < t_I^- + T, \\ 1 & \text{if } t \geq t_I^- + T, \end{cases} \quad (32)$$

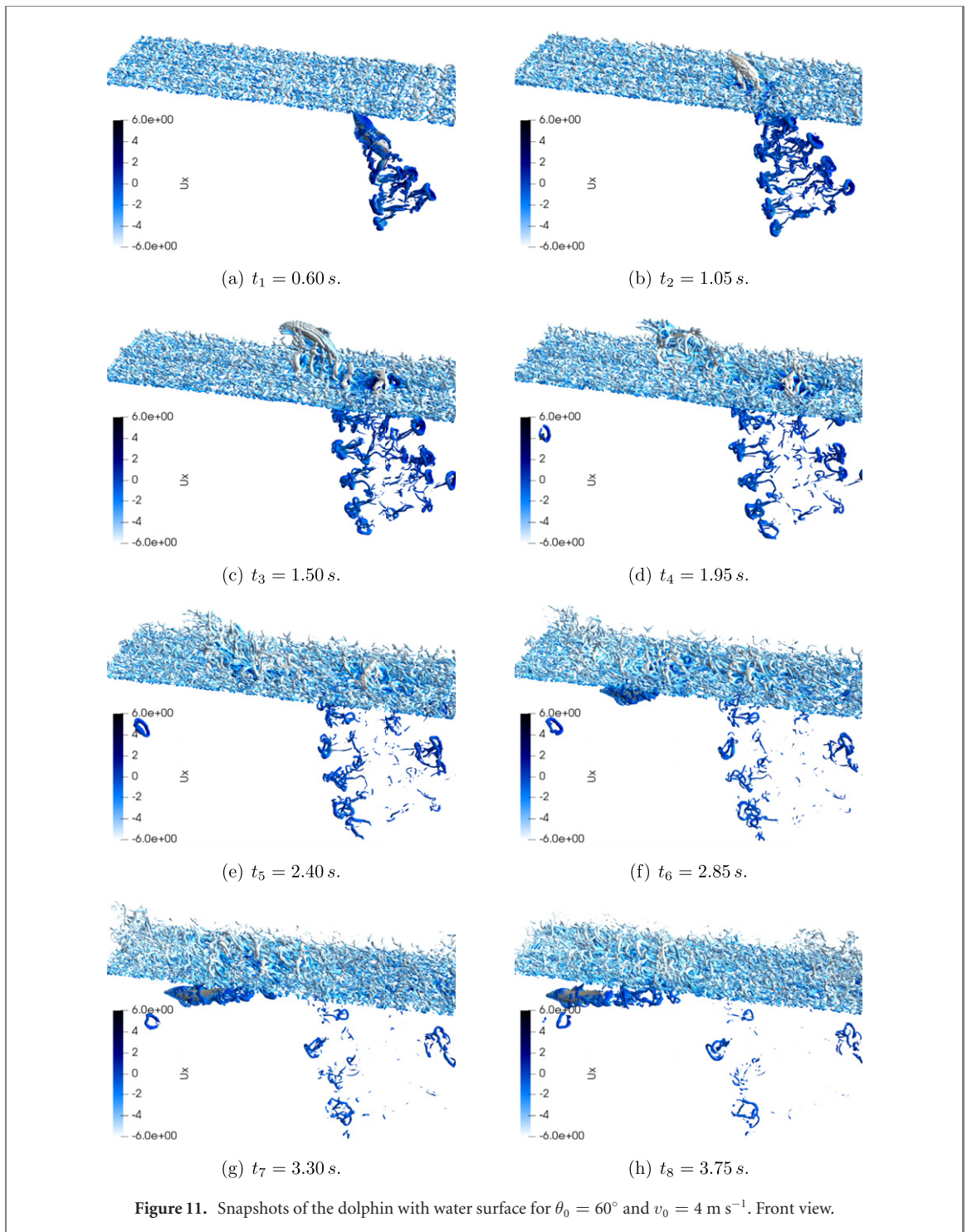
and the function  $q$  is linked to the position  $y_G$  of the dolphin's center of mass for  $t \leq t_I^-$ :

$$q(t) = \frac{1}{\max\left(1, \frac{1}{(10^{-4} + \min\text{mod}\{0.7(t-t_I^+), 1\} (y_G(t)-y_I^-))^2}\right)}, \quad (33)$$

where

$$\min\text{mod}\{a, b\} = \begin{cases} a & \text{if } |a| < |b|, ab > 0 \\ b & \text{if } |b| < |a|, ab > 0 \\ 0 & \text{otherwise.} \end{cases} \quad (34)$$

This handcrafted law has been developed from several numerical experiments to mimic as best as possible the dolphin's jump.



### 3.2. Results

A numerical simulation with  $\theta_0 = 60^\circ$  and  $V = 4 \text{ m s}^{-1}$  is performed using 256 processors. The initial air velocity is  $u(\mathbf{x}, 0) = -5 \text{ m s}^{-1}$  for  $(\mathbf{x}) \in \Omega_f^-$ .

The temporal evolution of functions  $p$  and  $q$  are given in figure 7(b), where the different times  $t_I^-$ ,  $t_I$ , and  $t_I^+$  and the other ones necessary to define functions  $p$  and  $q$  are plotted using vertical lines. These lines depend on the vertical position  $y_G$  of the dolphin's center of mass following (32) and (33) (see figure 7(a)). The periods with  $p(t) \geq 0$  are

highlighted in blue, and the period where  $q(t) \geq 0$  is highlighted in red. Blank zones thus denote an undeformed body shape.

Figure 8 shows the temporal evolution of the linear and angular position of the dolphin, the linear velocity, and the forces and torques exerted by the fluid on the body. The vertical velocity of the dolphin goes from  $v_G = 4 \text{ m s}^{-1}$  at  $t = 0 \text{ s}$  to  $v_G = 6.4 \text{ m s}^{-1}$  at  $t = t_I^+$  (see figure 8(b)). Note that we have chosen an initial velocity of  $v_G > 0$  to make use of a smaller computational domain. After this initial acceleration,

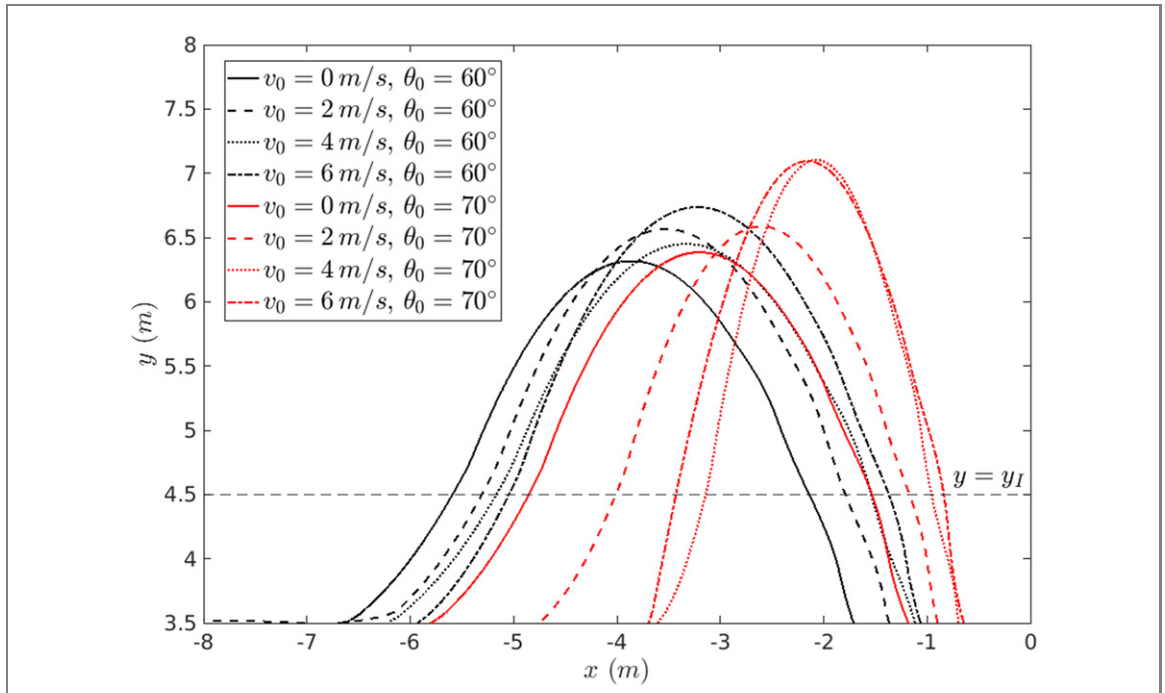


Figure 12. Comparison of the dolphin’s jump with different initial conditions  $v_0$  and  $\theta_0$ . The jump is from right to left.

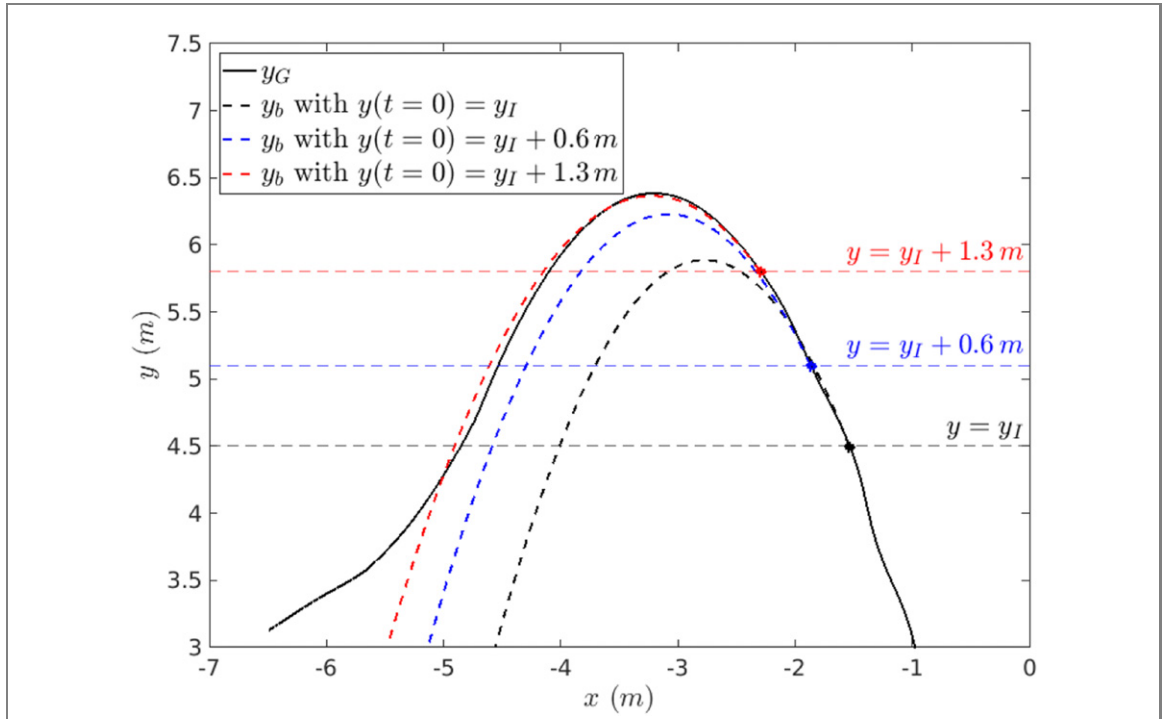


Figure 13. Comparison of the dolphin’s jump ( $v_0 = 4 \text{ m s}^{-1}$  and  $\theta_0 = 70^\circ$ ) with ballistic trajectories. The jump is from right to left.

the obtained velocity allows the dolphin to go out of the water (figure 8(a)). When the dolphin is in the air (in the red zone in figure 8), the dolphin’s vertical velocity  $v_G$  and the angle  $\theta_z$  start to decrease due to the gravity effect and the curvature. After re-entry into the water, a new sinusoidal swimming law is performed and the dolphin swims in the water with a position  $\theta_z \approx -10^\circ$  along which a slight acceleration is observed.

Eight snapshots  $\{S_i\}_{i=1,\dots,8}$  uniformly extracted during the actual numerical simulation are presented in figures 9–11. These snapshots correspond to  $\{t_i\}_{i=1,\dots,8}$  with  $t_i = 0.45(i - 1) + 0.6 \text{ s}$  and are plotted in figure 8 using vertical black lines. While figures 9 and 10 present visualisations of the dolphin’s jump through the surface of the water from different views, figure 11 presents snapshots of the Q-criterion.

The first two snapshots  $S_1$  and  $S_2$  correspond to the first periodic swimming law for propulsion. Snapshots  $S_3$  and  $S_4$  correspond to a period in the air where maximal curvature  $\bar{\kappa}$  is imposed. The fifth snapshot,  $S_5$ , is extracted for an almost undeformed body shape when re-entering the water. This deformation corresponds to  $q\bar{\kappa} = 0.007 \text{ m}^{-1}$  and  $p = 0$ . Finally, snapshots  $S_6$ ,  $S_7$ , and  $S_8$  correspond to the second periodic swimming law when the dolphin is back in the water. In the water, the vortices generated by the self-propelled dolphin are similar to those observed for most fish-like swimmers (Triantafyllou *et al* 2000, Zhu *et al* 2002, Liao *et al* 2003, Bergmann and Iollo 2016). Other kinds of vortices are generated in the shear layer at the water–air interface. Indeed, the initial water and air velocity are, respectively,  $u = 0 \text{ m s}^{-1}$  and  $u = -5 \text{ m s}^{-1}$ .

Trajectories of the dolphin's center of mass corresponding to different initial velocities  $v_0$  and angles  $\theta_0$  are presented in figure 12. As expected, the highest jumps correspond to the highest initial velocities. The correlation between the initial velocity and the jump cannot be easily determined. Indeed, the periodic swimming law is not stopped at the same time during the swimming stroke, thus influencing the jump velocity and angle at  $y = y_I$ .

In what follows, we compare the dolphin's jump with purely ballistic trajectories. The ballistic equations are:

$$\begin{cases} x_b(t) = x_0 + \bar{v}_0 t \cos(\alpha), \\ y_b(t) = y_0 + \bar{v}_0 t \sin(\alpha) - \frac{1}{2} g t^2, \end{cases} \quad (35)$$

where  $(x_0, y_0)$  is the initial projectile position,  $\alpha$  is the initial trajectory orientation at  $(x_0, y_0)$ ,  $\bar{v}_0$  is the initial velocity along the  $\alpha$  direction at  $(x_0, y_0)$ ,  $g = 9.81 \text{ m s}^{-2}$  is the gravity acceleration, and  $t$  is the time. Figure 13 shows the real dolphin's trajectory and several ballistic trajectories corresponding to different initial positions  $(x_0, y_0)$ .

For  $y_0 = y_I$  at  $t = 0.944 \text{ s}$ , i.e. when the dolphin's center of mass reaches the water's surface, large deviations between the dolphin and ballistic trajectories are observed. This is due to the fact that the dolphin is still accelerating (see figure 8). For  $y_0 = y_I^+ = y_I + 0.6 \text{ m}$  at  $t = 1.117 \text{ s}$ , the periodic swimming law is progressively stopped. A part of the dolphin is still in water, the acceleration is positive, and the deviation between the real trajectory and the ballistic trajectory is lower. Finally, for  $y_0 = y_I + 0.8 \text{ m}$  at  $t = 1.23 \text{ s}$ , the acceleration tends to decrease to zero and the ballistic trajectory almost perfectly matches the real dolphin's trajectory, until the dolphin goes back into the water at  $y_G = y_I$ . This is an obvious observation, since the forces exerted by the air on the dolphin ( $F_X \approx 6 \text{ N}$ , see figure 8) are quite low compared to the inertial effect of a 318 kg dolphin with velocity around  $6 \text{ m s}^{-1}$ .

## 4. Conclusions

In this paper, we have developed a numerical model of a dolphin's jump. This model deals with complex physical phenomena such as fluid–structure interactions and the liquid interface involving large deformations with possible topological changes (bubbles and droplets). The numerical model relies on fictitious domain approaches where the mesh used to solve the fluid does not follow the interfaces. The CSF method is used to model the water–air interface, and the VP method is used to take into account the dolphin's body. The numerical results are qualitatively in good agreement with dolphin jumps observed in nature. A dolphin has to generate large forces to reach a velocity threshold necessary for the jump. The jump is similar to a ballistic projectile where the resistive forces are neglected. This hypothesis is justified since the computed resistive forces are only around 6 N for a 320 kg dolphin with a velocity around  $6 \text{ m s}^{-1}$ . We are now working on optimizing the initial periodic swimming law to generate maximal acceleration to produce the highest jump.

## Acknowledgments

Computer time for this study was provided by the computing facilities MCIA (Mésocentre de Calcul Intensif Aquitain) of the Université de Bordeaux and of the Université de Pau et des Pays de l'Adour.

## Data availability statement

The data that support the findings of this study are available upon reasonable request from the authors.

## ORCID iDs

Michel Bergmann  <https://orcid.org/0000-0002-6122-7626>

## References

- Adalsteinsson D and Sethian J 1999 *J. Comput. Phys.* **148** 2–22
- Ahmadzadeh M, Saranjam B, Hoseini Fard A and Binesh A 2014 *Appl. Math. Modelling* **38** 1673–84
- Ahmed S, Bak S, McLaughlin J and Renzi D 2011 *SIAM J. Sci. Comput.* **33** 2402–20
- Angot P, Bruneau C and Fabrie P 1999 *Numer. Math.* **81** 497–520
- Aristoff J M, Truscott T T, Techet A H and Bush J W M 2010 *Phys. Fluids* **22** 032102
- Bale R, Hao M, Bhalla A, Patel N and Patankar N 2014 *Sci. Rep.* **4** 5904
- Barrett D, Triantafyllou M, Yue D, Grosenbauch M and Wolfgang M 1999 *J. Fluid Mech.* **392** 182–212
- Beal D, Hover F, Triantafyllou M, Liao J and Lauder G V 2006 *J. Fluid Mech.* **549** 385–402
- Bergmann M, Cordier L and Brancher J P 2006 *Phys. Fluids* **18** 028101
- Bergmann M, Hovnanian J and Iollo A 2014a *Commun. Comput. Phys.* **15** 1266–90



- Bergmann M and Iollo A 2011 *J. Comput. Phys.* **230** 329–48
- Bergmann M and Iollo A 2016 *J. Comput. Phys.* **323** 310–21
- Bergmann M, Iollo A and Mittal R 2014b *Bioinspiration Biomimetics* **9** 046001
- Bhalla A P S, Bale R, Griffith B E and Patankar N A 2014 *J. Comput. Phys.* **256** 88–108
- Bhalla A P S, Griffith B E and Patankar N A 2013 *PLoS Comput. Biol.* **9** e1003097
- Bozkurttas M, Tangorra J, Lauder G and Mittal R 2009 *Mining Smartness from Nature (CIMTEC 2008) Mining Smartness from Nature (CIMTEC 2008)* vol 58 (Zurich: Trans Tech Publications) pp 193–202
- Brackbill J, Kothe D and Zemach C 1992 *J. Comput. Phys.* **100** 335–54
- Chang B, Myeong J, Virost E, Clanet C, Kim H Y and Jung S 2019 *J. R. Soc. Interface* **16** 20190014
- Chorin A 1968 *Math. Comp.* **22** 745–62
- Cox R 1986 *J. Fluid Mech.* **168** 169–94
- Fish F E, Nicastrò A J and Weihs D 2006 *J. Exp. Biol.* **209** 590–8
- Fish F and Lauder G 2006 *Annu. Rev. Fluid Mech.* **38** 193–224
- Gao A and Triantafyllou M S 2018 *J. Fluid Mech.* **850** 304–35
- Gopalkrishnan R, Triantafyllou M S, Triantafyllou G S and Barrett D 1994 *J. Fluid Mech.* **274** 1–21
- Gray J 1936 *J. Exp. Biol.* **13** 192–9
- Han P, Wang J, Fish F E and Dong H 2020 Kinematics and hydrodynamics of a dolphin in forward swimming *AIAA AVIATION 2020 FORUM* (June 15–19), <https://doi.org/10.2514/6.2020-3015>
- Jiang G S and Shu C W 1996 *J. Comput. Phys.* **126** 202–28
- Kern S and Koumoutsakos P 2006 *J. Exp. Biol.* **209** 4841–57
- Li G, Kolomenskiy D, Liu H, Thiria B and Godoy-Diana R 2022 *Front. Robot. AI* **9** 825889
- Liao J, Beal D, Lauder G and Triantafyllou M 2003 *Science* **302** 1566–9
- Lighthill M 1970 *J. Fluid Mech.* **44** 265–301
- Liu X D, Osher S and Chan T 1994 *J. Comput. Phys.* **115** 200–12
- Luddens F, Bergmann M and Weynans L 2015 *Int. J. Numer. Methods Fluids* **79** 654–75
- Maertens A P, Gao A and Triantafyllou M S 2017 *J. Fluid Mech.* **813** 301–45
- Mendelson L and Techet A H 2020 *Bioinspiration Biomimetics* **16** 016006
- Mittal R, Dong H, Bozkurttas M, Najjar F, Vargas A and von Loebbecke A 2008 *J. Comput. Phys.* **227** 4825–52
- Mittal R and Iaccarino G 2005 *Annu. Rev. Fluid Mech.* **37** 239–61
- Nangia N, Griffith B E, Patankar N A and Bhalla A P S 2019a *J. Comput. Phys.* **390** 548–94
- Nangia N, Johansen H, Patankar N A and Bhalla A P S 2017 *J. Comput. Phys.* **347** 437–62
- Nangia N, Patankar N A and Bhalla A P S 2019b *J. Comput. Phys.* **398** 108804
- Osher S and Sethian J A 1988 *J. Comput. Phys.* **79** 12
- Patankar N A 2003 *Langmuir* **19** 1249–53
- Pavlov V 2006 *Bioinspiration Biomimetics* **1** 31–40
- Peskin C 1972 *J. Comput. Phys.* **10** 252–75
- Riedeberger D and Rist U 2012 *High Performance Computing in Science and Engineering '11* ed W E Nagel, D B Kröner and M M Resch (Berlin: Springer) pp 379–91
- Russo G and Smereka P 2000 *J. Comput. Phys.* **163** 51–67
- Sethian J A 1999 *Level Set Methods and Fast Marching Methods* (Cambridge: Cambridge University Press)
- Sethian J 1996 *Appl. Math.* **93** 1591–5
- Shirgaonkar A A, MacIver M A and Patankar N A 2009 *J. Comput. Phys.* **228** 2366–90
- Smits A J 2019 *J. Fluid Mech.* **874** P1
- Sussman M, Smereka P and Osher S 1994 *J. Comput. Phys.* **114** 146–59
- Tanaka H, Li G, Uchida Y, Nakamura M, Ikeda T and Liu H 2019 *PLoS One* **14** e0210860
- Temam R 1969 *Arch. Ration. Mech. Anal.* **32** 377–85
- Triantafyllou M S, Techet A H, Zhu Q, Beal D N, Hover F S and Yue D K P 2002 *Integr. Comparative Biol.* **42** 1026–31
- Triantafyllou M, Triantafyllou G and Yue D 2000 *Annu. Rev. Fluid Mech.* **32** 33
- Truscott T T, Epps B P and Belden J 2014 *Annu. Rev. Fluid Mech.* **46** 355–78
- von Loebbecke A, Mittal R, Fish F and Mark R 2009a *Hum. Mov. Sci.* **28** 99–112
- von Loebbecke A, Mittal R, Fish F and Mark R 2009b *J. Biomech. Eng.* **131** 054504
- von Loebbecke A, Mittal R, Mark R and Hahn J 2009c *Sport. Biomech.* **8** 60–77
- Vreman A 2004 *Phys. Fluids* **16** 3670–81
- Zhu Q, Wolfgang M, Yue D and Triantafyllou M 2002 *J. Fluid Mech.* **468** 1–28